25th ABCM International Congress of Mechanical Engineering
October 20-25, 2019, Uberlândia, MG, Brazil

# COB-2019-1531

# NUMERICAL STUDY OF FLOW AROUND OSCILLATING SIMPLE GEOMETRIES USING POROUS MEDIUM

**Gustavo de Goes Gomes**
Universidade de São Paulo, USP - Avenida Prof. Almeida Prado, 1280 - Butantã, São Paulo - SP, 05508-900
Instituto de Pesquisas Tecnológicas, IPT - Avenida Prof. Almeida Prado, 532 - Butantã, São Paulo - SP, 05508-280
gustavo.gomes@usp.br

**João Lucas Dozzi Dantas**
Instituto de Pesquisas Tecnológicas, IPT - Avenida Prof. Almeida Prado, 532 - Butantã, São Paulo - SP, 05508-280
jdantas@ipt.br

**Gustavo Roque da Silva Assi**
Universidade de São Paulo, USP - Avenida Prof. Almeida Prado, 1280 - Butantã, São Paulo - SP, 05508-900
g.assi@usp.br

***Abstract.*** *This paper presents an initial CFD analysis using a porosity model to represent the hydrodynamic perturbation of disks under forced oscillations in a simplified way. The oscillation is used to represent a subsea equipment in a lifting, or deploying process, under a ship heave motion. The disks are, initially, solid (porosity equals to 0), in order to validate the model, and later porosity is added. The disk is forced to oscillate under a sinusoidal motion inside water. The Keulegan-Carpenter number, KC, in relation to its diameter, spans from 0.25 to 1.50, and the set porosity is 5%. The added mass and damping coefficients are calculated from the obtained hydrodynamic forces, and compared with experimental data present in the literature. For the porosity scenarios, a porous medium model is adopted rather than the actual geometry of perforated disks, the hydrodynamical forces are calculated, and the permeability coefficients are set in a iterative manner. The differences in flow patterns are then analyzed. It is expected in future works that with this study it will be able to simulate bodies with greater complexity with meaningful force outputs and accessible computational cost.*

***Keywords:*** *Oscillating flow, Porous medium, Damping, Added mass, Numerical study*

## 1. INTRODUCTION

As the offshore oil production reaches increasingly deeper fields, the use of large subsea equipment became more common. That can be due to difficulties implied by the distance from the oil field to the platform, the increased motions of the floating production units, or also because it is a more cost efficient production alternative, in comparison to fixed or floating production in deep waters (Wadhwa and Thiagarajan, 2009). This kind of equipment can be composed of manifolds, PLETs, PLEMs, wet christmas trees, among others.

A large proportion of the costs and risks of an offshore field development, even more for the deep water case, are related to the process of deployment/lift and installation/decommissioning of the subsea equipment. This process requires special vessels with well dimensioned cranes in relation to the size and weight of the equipment. Still, the operation must be done under an operable window, due to the weather conditions. So, in order to do a safe operation it is required knowledge on the weather, including wind and waves, the vessel′s induced response and, also, the equipment hydrodynamics (Minguez *et al.*, 2015). The vessel′s response due to the environmental conditions can impose motion on the lifted equipment, which can change the loads and tensions on the crane system. Due to the phase difference in the oscillations of the vessel and of the equipment, resonance in the cables may also occur. Knowledge on the equipment hydrodynamics is important not only due to this kind of motion, but also due to marine currents and the interaction with the seafloor and water surface.

In this paper, the main interest relies on simple bluff body geometries, under sinusoidal oscillations, which can represent, for instance, the imposed motion on the mentioned equipment due to the vessel′s heave motion. For more complex geometries, such the subsea equipment of the offshore industry, it is more common to obtain the coefficients with model experiments, instead of numerical simulations, as seen in (Kjemperud, 2011). One of the reasons for that is due to the augmented geometry complexity, which would lead to additional computational cost. In this work for more complex geometries, a porous region model approach is adopted, and to obtain the permeability coefficients an iterative method is used.

The present study exploits series of numerical forced oscillation experiments on one simple geometry type: disks. For the simulations, there is movement only in the axial direction of the disk. The numerical experiments span on a range of low KC numbers from 0.25 to 1.50, relative to its diameter, with a solid and a 5% porosity disk. For the simulations only one value of the coefficient $\beta$ was used, due to the weak relation between the frequency and the hydrodynamic coefficients for low KC numbers in this kind of geometry, as presented by (Tao and Dray, 2008). Both coefficients are better presented in the subsequent sections. The numerical simulations are done using the commercial software ANSYS Fluent version 19.2. The difference from other papers in the same subject is the approach used for the simulations with porosity. Instead of changing the geometries in the simulations, for example, adding holes in the disk to increase its porosity, the idea here is to keep the simple geometry volume and use the porous region model to obtain reasonable coefficients. For the last part of the study, the interest lies on the flow pattern changes due to the adoption of the porosity model, along with the variation of KC.

## 2. OBJECTIVE

This paper aims to present a first analysis of a simplification on CFD forced oscillation simulations using porous media. Porous media is employed in this case to replace the full body geometry. This first investigation is focused, not only, on the comparison of forces, and consequently, hydrodynamic coefficients, but also, flow pattern changes due to different porosity and KC.

## 3. CASE STUDIES

In the present paper two cases are studied: a solid and a 5% porosity disk.

The geometry used in the simulations is the same one employed by Tao and Dray (2008), which is a disk with diameter, $d$, of 400 mm and thickness, $a$, of 8 mm. The KC used ranges from 0.25 to 1.50, with maximum velocity, $U_M$, ranging from 0.025 to 0.15 m/s, which gives a maximum Reynolds number of $6.0 \times 10^4$ and a transition regime between laminar and turbulent flow. Figure 1 schematically shows the dimensions and the motions of the plate used, and the experimental apparatus used by Tian *et al.* (2017).

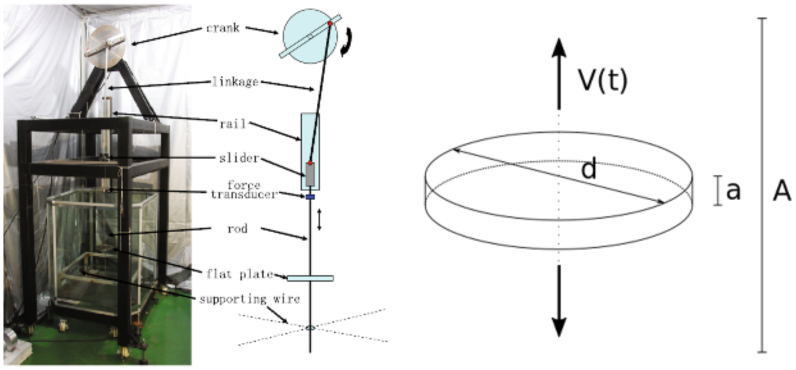

Figure 1. Experimental apparatus from (Tian *et al.*, 2017) (left), and disk motion (right)

In the first study case, the simulations are done over a solid flat circular plate, and the non-dimensional coefficient results are measured and compared with experimental data found in (Tao and Dray, 2008) and (Tian *et al.*, 2017). This first set of simulations are done in order to verify the proposed numerical model, and to compare the force outcome differences, due to different turbulent models, time-steps and mesh sizes. In order to reduce the discretization error, a grid convergence study is conducted for six geometrically similar grids, in an analogous method employed by (Eça *et al.*, 2010).

In the grid study six meshes, alongside with six different time steps are used, the values of number of cells, cell height and time step are presented in Tab. 1. Mesh M05 was used only in one scenario. The meshes are in accordance with the adopted by Tao and Thiagarajan (2003), the differences are mainly due to geometry changes.

Figure 2 presents the mesh M2. In the figure, the blue line shows the symmetry boundary layer, in the disk axial direction, whereas the green lines show the pressure outlet boundaries. Since the approach taken is to use a reference frame motion for the entire domain, there is always backward flow in the simulations depending on the direction of the movement. It is important to point out that the domain motion occurs on the axial direction of the disk, *i.e.* in the horizontal direction of the figure.

For the second study case, simulations are done with porosity, therefore, the empty disk region was replaced by a grid, similar in size with the one near the plate walls. In this new region the porous media model was set. According to ANSYS (2018), there are some limitations on the porosity model, *e.g.* the effect of turbulence inside the media. The focus of this

Table 1. Mesh sizes and time steps used in the grid convergence study

| Mesh | Refinement ratio ($h_i/h_1$) | Time step ratio ($\tau_i/\tau_1$) | Number of cells | Cell height near wall [mm] | Time step [s] |
|---|---|---|---|---|---|
| M05 | $1/\sqrt{2}$ | $1/2$ | 285441 | 0.0017677 | 0.000625 |
| M1 | 1 | 1 | 141729 | 0.0025 | 0.00125 |
| M2 | $\sqrt{2}$ | 2 | 70308 | 0.0035355 | 0.0025 |
| M3 | 2 | 4 | 34869 | 0.005 | 0.005 |
| M4 | $2\sqrt{2}$ | 8 | 16974 | 0.0070710 | 0.01 |
| M5 | 4 | 16 | 8439 | 0.01 | 0.02 |

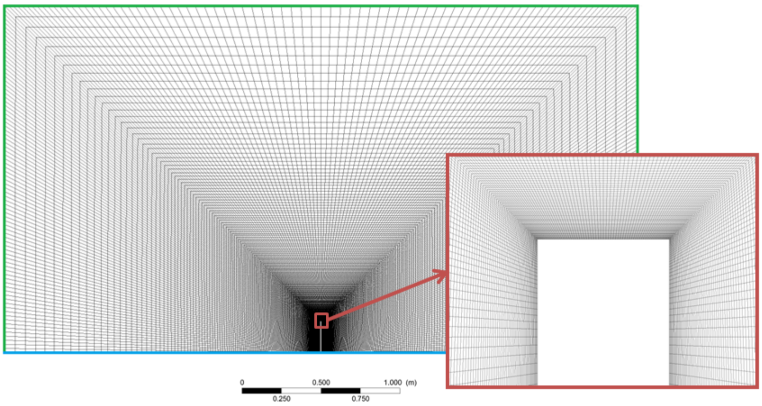

Figure 2. M2 mesh

study case is to obtain the permeability tensors for the simulations. In order to do so, an iterative approach is used, in which the simulations are done in the same operating conditions as for the solid plate case, the results are compared with experimental data for porous disks by the same authors as before, and the tensors are updated.

## 4. METHOD

For flow past bluff bodies that undergo sinusoidal oscillations, the generated flow structure depends mainly on the non-dimensional Keulegan-Carpenter (KC) and $\beta$, (Tatsuno and Bearman, 1990). $\beta$ can be viewed as the quotient of the Reynolds number, Re, by KC. Equations (1), (2) and (3) present KC, Re and $\beta$, respectively.

$$KC = \frac{U_M T}{L} = \frac{2\pi A}{L} \tag{1}$$

$$Re = \frac{U_M L}{\nu} \tag{2}$$

$$\beta = \frac{L^2}{\nu T} = \frac{Re}{KC} \tag{3}$$

Being A the amplitude of the motion, L a characteristic length, and T the oscillation period. $U_M$ can be expressed as $U_M = A\omega$, with $\omega$ being the circular frequency of the movement, and equal to $2\pi A/T$. Moreover, according to Keulegan and Carpenter (1958), forces on oscillatory motion can be more accurately described by the Morison equation, Eq. (4).

$$F = \frac{1}{2} C_d \, \rho \, S \, |U| U + \rho \, C_M \forall \, \dot{U} \tag{4}$$

In which S is the projected area and $\forall$ is the immersed volume of the body. In Eq. (4), force is expressed by two components, the first one due to drag, and so related to the squared velocity, and the second due to acceleration of the fluid, or its inertia. To represent the force in this way, there is the necessity of including two coefficients: drag, $C_d$, and inertia coefficient, $C_M$, (Sarpkaya and Isaacson, 1981). The $C_M$ coefficient can be expressed in terms of the added mass coefficient, $C_a$, by $C_M = 1 + C_a$.

In (Keulegan and Carpenter, 1958) it is shown how to obtain $C_d$ and $C_M$ using Fourier analysis, for similar sinusoidal motion experiments. In the literature there are series of experiments and numerical simulations that focus on obtaining both coefficients for different geometries, sizes, porosities, motions, and consequently, different numbers of KC and $\beta$.

For the simulations, the geometry motion is set by Eq. (5), in the axial direction for the disk.

$$\zeta(t) = A\cos(\omega t) \tag{5}$$

To set the mesh frame motion on the software, however, the correspondent velocity had to be used, as given by Eq. (6).

$$U(t) = -A\omega\sin(\omega t) \tag{6}$$

The values of A and $\omega$ vary with KC and $\beta$. For both sets of simulations $\omega$ and $\beta$ remained constants, with T equals to 4 s, and, consequently, $\omega = \pi/2$ and $\beta$ approximately 4e+4.

The non-dimensional coefficients, $C_d$ and $C_a$, are obtained in a similar way as presented by (Tao and Dray, 2008), (Sarpkaya and Isaacson, 1981) and consequently (Keulegan and Carpenter, 1958), but since the phase movement set in this work is different from the previous authors, the coefficient calculation has differences due to the phase, as presented by Eqs. (7) and (8).

$$C_d = \frac{3\omega}{4\rho S U_M^2}\int_0^T F(t)\sin(\omega t)dt \tag{7}$$

$$C_a = \frac{1}{\pi\rho\forall U_M}\int_0^T F(t)\cos(\omega t)dt \tag{8}$$

Non-dimensionalization is used in order to compared similar models with different sizes, working fluids, velocities and frequencies. To be able to compare the results with the previously mentioned authors, further non-dimensionalization is required and presented by Eqs. (9) and (10), in which m′ is the theoretical ideal fluid added mass.

$$A' = \frac{C_a m}{m'} \tag{9}$$

$$B' = \frac{KC\, C_d}{4\pi} \tag{10}$$

### 4.1 NUMERICAL MODELING

The numerical simulations were done using the commercial software ANSYS Fluent, version 19.2 with double precision. The flow field is modeled as a single incompressible fluid, isothermal, in two dimensions with an axisymmetric domain, and the unsteady Reynolds-averaged Navier-Stokes (uRANS) equations are solved. The fluid used is liquid water with density, $\rho$, and dynamic viscosity, $\mu$, equals to 998.2 $kg/m^3$ and 0.001003 $kg/ms$, respectively.

The forced oscillations are done over the entire domain using a reference frame motion, which simplifies the problem, and avoids mesh changes throughout the simulation. The motion is set by a compiled user-defined function for the velocity movement. The same approach was used by (Ghozlani *et al.*, 2012) and (Dütsch *et al.*, 1998), and is presented as follows. Due to the motion, the fundamental fluid mechanics equations had to be changed into an accelerated reference frame, in which $x_i$ is the inertial frame and $\tilde{x}_i$ is the accelerated frame. The connection between both is given by Eq. (11).

$$x_i = \tilde{x}_i + x_{i,s} \tag{11}$$

In which $x_{i,s}$ denotes the position of the accelerated frame. Differentiating Eq. (11) results in the velocity equations for each frame, shown by Eq. (12).

$$u_i(x_i,t) = \tilde{u}_i(\tilde{x}_i,t) + U_{i,s}(t) \tag{12}$$

Thus, the continuity and momentum equations in the accelerated system are Eq. (13) and Eq. (14).

$$\frac{\partial\tilde{u}_i}{\partial\tilde{x}_i} = 0 \tag{13}$$

$$\rho\left(\frac{\partial\tilde{u}_i}{\partial t} + \tilde{u}_j\frac{\partial\tilde{u}_i}{\partial\tilde{x}_j}\right) = -\frac{\partial\tilde{p}}{\partial\tilde{x}_i} + \mu\left(\frac{\partial^2\tilde{u}_i}{\partial\tilde{x}_j^2}\right) - \rho\frac{dU_{i,s}(t)}{dt} \tag{14}$$

Being the last term in right hand side of Eq. (14) a sink term that considers the acceleration of the body.

Since the maximum Reynolds number is in a transition region, two different turbulence models and a laminar approach were adopted. The turbulence model $k - k_L - \omega$ was used, due to its capability of simulating the transition. It is a 3 equation model, based on the $k - \omega$ framework, with an additional equation for the laminar kinetic energy, $k_L$, (Walters and Cokljat, 2008). Another option to simulate transition would be using the model known as $\gamma - Re_\theta$, but it was not chosen due to the use of a non-inertial reference frame, which could lead to a violation of the Galilean invariance, a known deficiency of the model, (Menter *et al.*, 2006). The shear-stress transport-model, also known as $k - \omega-$ SST, was also employed, because it is a widely used model and a good source to compare the results with a model that assumes fully turbulent flow. It is a 2 equation model that uses the $k - \omega$ model near the wall boundaries and the $k - \epsilon$ in the wake and free-stream regions of the flow, (Menter, 1994).

For the simulation cases in which the porosity model is used, an additional sink term, Eq. (15), is applied to the momentum equation (ANSYS, 2018).

$$S_i = -(\sum_{j=1}^{2} D_{ij}\mu U_j + \sum_{j=1}^{2} C_{ij}\frac{1}{2}\rho|U|U_j) \tag{15}$$

In which the $i^{th}$ terms are related to (x or y) momentum equations, U is the velocity, D and C are second order tensors, related to the region permeability. The first term on the right handside in eq. (15) represents a viscous loss term, and can be viewed as a pressure loss due to the Darcy′s law, the second term is an inertial loss term, related to drag inside the porous region, which is similar to the Forschheimer correction for high Reynolds number flows in relation to the pore dimension, as presented by Das *et al.* (2018). For a saturated porous medium flow with low velocity and $Re$ related to the pore diameter below 1, the second term can be neglected, since the velocity is squared, whereas when the velocity is high enough, the first term can be neglected. The second part of this work focuses on obtaining the tensors C and D for the porous disk.

Another change in the momentum equations and also in the continuity equation, is due to the porosity effect. In a more simplistic approach it appears only on the time-derivative terms, as $\frac{\partial}{\partial t}$ $(\gamma\ \rho\ \phi)$, in which $\phi$ is a scalar quantity and $\gamma$ the porosity. On other approaches it is accounted in all other terms, changing also the sink terms in Eq. (15).

The first approach taken for the porous disk simulations was to avoid the superficial velocity calculation for the porous media, which is more commonly used, and adopt the physical velocity calculation. This alternative is more accurate since the 'true' velocity is calculated inside the region and porosity is accounted for the convection and diffusion terms in the transport equations. When this approach was used, however, the simulations did not achieve convergence for small porosity values, but for higher values instead, which are not the main concern of this paper. For this reason, the superficial velocity approach had to be adopted.

In this way, a superficial velocity is used inside the porous medium, based on the volumetric flow rate, to ensure continuity of the velocity vectors across the medium interface, (ANSYS, 2018). This velocity can be represented by Eq. (16), in which $\gamma$ is the porosity value.

$$\overrightarrow{U}_{superficial} = \gamma \overrightarrow{U}_{physical} \tag{16}$$

As mentioned before, superficial velocity values within the porous region remain the same as those outside the region, and porosity is not taken into account in the differential terms of the transport equations, (ANSYS, 2018), which can be another limitation of the model.

In order to calculate the forces generated by the porous plate movement only the pressure difference was considered in the surfaces normal to the movement and not the shear stress at the edges, parallel to the flow. This can be done since the disk has low thickness in comparison to its diameter, and so, the force components due to pressure are orders of magnitude larger than the shear component. The force was calculated using the pressure integral over the two sides of the disk, as shown by Eq. (17), in which $p$ is the pressure and $\overrightarrow{n}$ is the normal vector of face $S$.

$$\overrightarrow{F} = \sum_{1}^{2} \int_S p\overrightarrow{n}\, da \tag{17}$$

## 4.2 PERMEABILITY COEFFICIENTS

The permeability coefficients, $D_{ij}$ and $C_{ij}$, in the software are diagonal matrices, so, four parameters had to be set, called here $d_{11}$ and $d_{22}$, for the viscous terms, $c_{11}$ and $c_{22}$ for the inertia terms. Since the flow in the experiments only pass through the disk by its holes, the coefficients were set assuming that the flow inside the porous medium would, preferably, have an horizontal motion. To do this $d_{22}$ was, at least, one order of magnitude larger than $d_{11}$, and $c_{22}$, at least, two orders of magnitude than $c_{11}$. The flow velocity is small for the selected KC values, thus the inertial terms had little contribution in the Eq. (15) in relation to the viscous terms. For this reason as an initial guess $c_{11}$ had a value of order e+1. Changes in the value, altered the results, mainly, for higher values of KC. Since, the major interest in the paper is for flows with low KC numbers and with a horizontal preferred direction, parameter $c_{11}$ had most significance.

The approach taken to find the parameters was to find first an appropriate value for $c_{11}$, and then make changes in the other parameters to reach acceptable values for the coefficients A' and B'.

## 5. VALIDATION

In order to reduce discretization error, $\varepsilon$, in the simulations of the solid disk a grid convergence study was conducted for 5 geometrically similar meshes and 5 different time steps.

According to ASME (2009) discretization error can be defined as the error between the solution and the obtained solution for a "infinite refined" mesh. Since it is not possible to achieve an "infinite refined" mesh, an extrapolation method is used instead, in which some number of geometrically similar meshes are used, and, preferably, an integral local quantity, $\varphi_i$, is compared between the simulations. Then a extrapolation method is used to estimate the value of the local quantity at the "infinite refined" mesh, $\varphi_0$.

For simpler cases, ASME (2009) recommends the use of Richardson extrapolation method. However, since the problem under discussion is complex, which adopts uRANS equations in an accelerated coordinate system, instead, it is used the least squares extrapolation proposed by Eça *et al.* (2010). For the estimation of the discretization error Eq.(18) must be solved.

$$\varepsilon \cong \delta_{RE} = \varphi_i - \varphi_o = \alpha_x h_i^{p_x} + \alpha_t \tau_i^{p_t} \tag{18}$$

In which $\delta_{RE}$ is the discretization error obtained by the Richardson extrapolation, $\alpha_x$ and $\alpha_t$ are both constants, $p_x$ and $p_t$ are the observed orders of accuracy of both space and time, respectively, $h_i$ is the typical cell size and $\tau_i$ is the time step. According to (Eça *et al.*, 2010), it is possible to replace the two terms on the right hand-side by a single term which combines the spatial and time discretizations, if $h_i$ and $\tau_i$ are chosen in a consistent way, according to the order of accuracy of each term. For this reason, as the grid factor used for the generation of new grids was $\sqrt{2}$, and since the time integration used in the simulations is only first-order accurate, the time step ratio had to be 2. In this way it is possible to use Eq. (19) instead of Eq. (18).

$$\varepsilon \cong \delta_{RE} = \varphi_i - \varphi_o = \alpha \lambda^p \tag{19}$$

As reported by Eça *et al.* (2015), the advantages of using Eq. (19) in relation to Eq. (18) is that the minimum number of data points is smaller, only 3, and it is possible to use the same procedure developed for steady flows. On the other hand, it is not possible to distinguish which discretization error is predominant, space or time.

In order to have a better estimation of the numerical uncertainty it was also used the Grid Convergence Index (GCI), a 95% prediction interval for the obtained extrapolation and the standard deviation of the results in each of the final plate oscillations, $s$. GCI is an uncertainty estimator that uses a safety factor, $F_S$, depending on the order of accuracy of the extrapolation for $\varepsilon$. According to Eça *et al.* (2010), if the observed order of accuracy is near the formal order of accuracy, in other words, the results are in the asymptotic region, $F_S = 1.25$, differently, $F_S = 3$. The term $p$ in Eq.(19), is said to be in the formal order of accuracy if $0.95 \leq p \leq 2.05$. The prediction interval was set according to the standard deviation of the extrapolation errors in relation to the simulated data, $\sigma$. Assuming a normal distribution, the 95% prediction interval can be set as in (Meeker *et al.*, 2017) as $\varphi(r) \pm 1.96\ \sigma$, with $\varphi(r)$ being the value of the extrapolation and $r$ the ratio of the mesh to the most refined mesh used, $r = h_i/h_1$. In this way, assuming that there is no co-variance between each of the three sources of error, the numerical uncertainty can be given as eq.(20).

$$U_\varphi = \sqrt{(\varepsilon\ F_S)^2 + (1.96\ \sigma)^2 + s^2} \tag{20}$$

The initial results with the $k - k_L - \omega$ model showed good agreement for $p$ in the formal order of accuracy only for higher KC values, 1.25 and 1.5, for the lowest values, the results were a scatter of points. Taking a closer look to the simulation results, it was possible to see that the flow pattern was asymmetric in relation to the motion of the disk. In other words, the flow pattern saw when the disk was in one movement extreme was not similar to the following extreme.

Figure 3 shows a comparison between the force results for the meshes M1 and M5 with KC of 0.25 and the displacement of the disk. From the figure it is possible to see that the M1 peak results are lower than the M5 results, and M1 trough results are still lower than M5. It is, also, possible to see that the values of peaks and troughs for the M5 results are much more similar, in absolute value, than the M1 values. Figures 4 and 5 show the velocity magnitude of the simulations for both meshes in four different times in the same period of oscillation.

In the figures, each frame can be understood as:

- 1st Frame - Velocity $= -U_M$ and displacement $= 0$;
- 2nd Frame - Velocity $= 0$ and displacement $= -A$;
- 3rd Frame - Velocity $= U_M$ and displacement $= 0$;
- 4th Frame - Velocity $= 0$ and displacement $= A$.

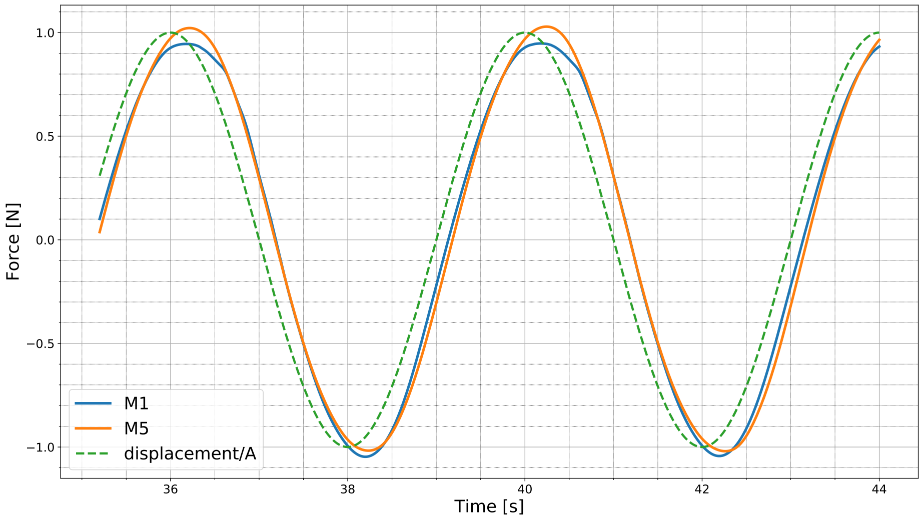

Figure 3. Force results comparison for M1 and M5 with KC = 0.25 and the displacement of the disk

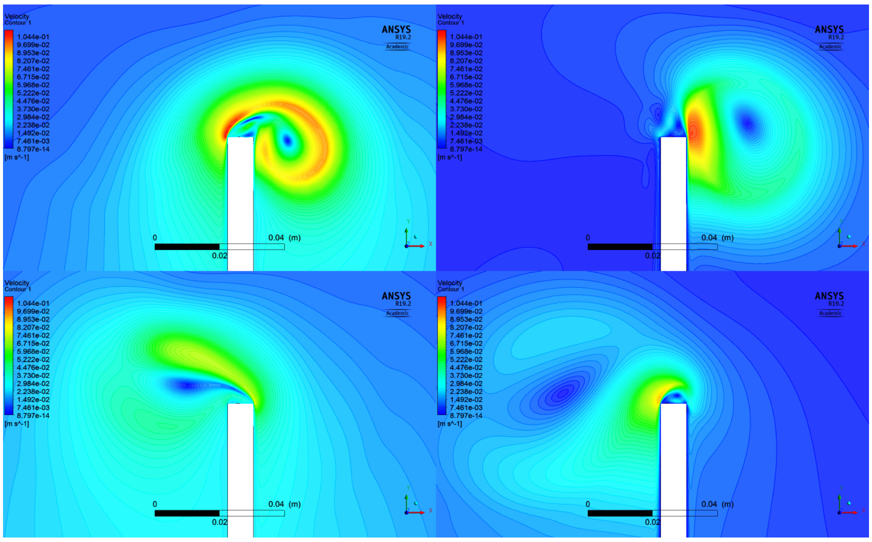

Figure 4. Velocity field of the M1 simulation with KC = 0.25 using the $k - k_L - \omega$ model

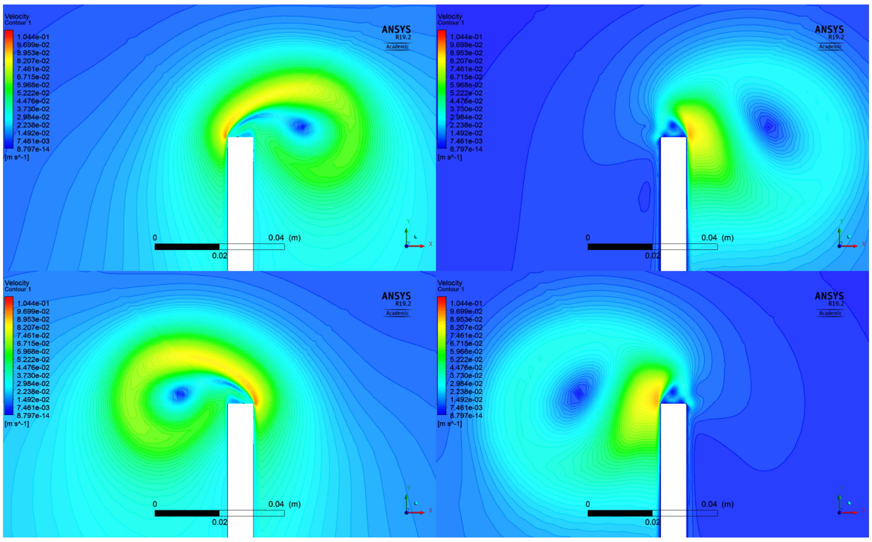

Figure 5. Velocity field of the M5 simulation with KC = 0.25 using the $k - k_L - \omega$ model

From Fig. 4 the asymmetry in the M1 flow pattern in the same period of oscillation is visible, and the opposite can be said for the M5 flow in Fig. 5. Similar asymmetric results occurred also with the meshes M2 and M3 for the lower values of KC. As the value increased, the asymmetry was smoothed. Because of that the grid convergence study of the lower values of KC, mesh M5 was not used, and for KC of 0.25 a more refined mesh had to be created, mesh M05. For the $k-\omega-$SST model, the results showed lower levels of asymmetry when compared with the previous model.

The results of the grid convergence study for the laminar simulations are not shown in the following figures. In those simulations, due to the use of less dissipative equations, in comparison with uRANS, the vortex generated by the end of the plate in one period of oscillation often interacted with the subsequent vortexes, thus interfering in the force curve. Due to this, the coefficient results had high variance, in comparison with the results of the turbulence model simulations.

Some of the results for the grid convergence study are presented in Fig. 6, which the error bars are equal to $U_{\varphi i}$, and $p$ is assumed, with good agreement, to be equal to 2. Not all results are presented in order to save space. Comparing all the results, most of the times the error bars are smaller when using the $k-k_L-\omega$ model.

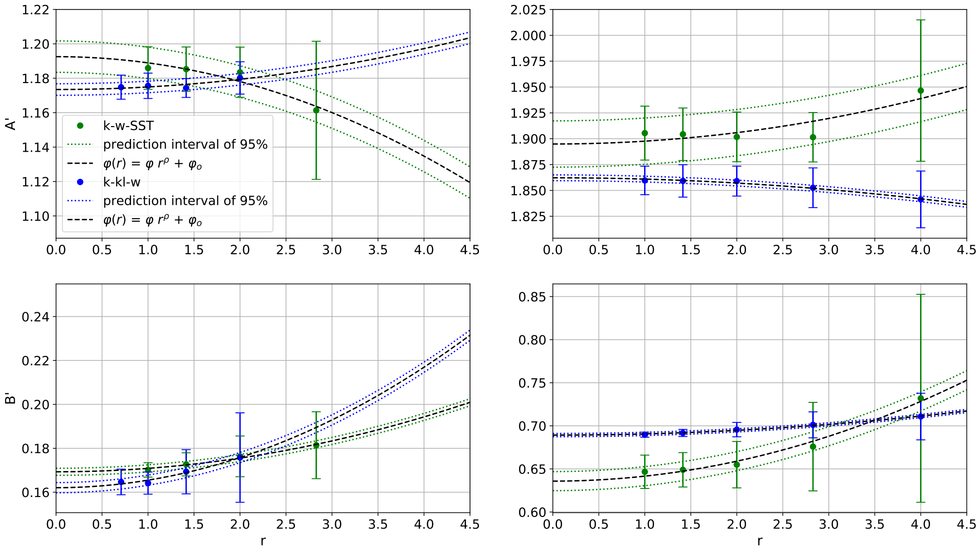

Figure 6. Grid convergence study for KC=0.25 (left) and KC=1.50 (right)

## 6. RESULTS AND DISCUSSION

### 6.1 STUDY CASE: SOLID DISK

The results for the simulations with mesh M2 for solid disks and KC ranging from 0.25 to 1.50 are presented with the experimental results of (Tao and Dray, 2008) and (Tian *et al.*, 2017) in Fig. 7, the error bars in the numerical results are equal to $U_{\varphi i}$, obtained previously. From the figure, it is possible to see better agreement with both non-dimensional coefficients for the simulations with $k-k_L-\omega$. The error bars for the laminar simulations were one order of magnitude larger than the other two, the main reason for that was the high values of variance in the results. Mesh M2 was chosen because it achieved good results with less computational effort than M1, or M05, and with acceptable levels of uncertainty.

### 6.2 STUDY CASE: 5% POROUS DISK

For the simulations with porosity, mesh M2, with the same time step used before, was chosen, since it achieved good results with feasible computational cost and uncertainty level. As a result of the porous region, the total amount of cells in the mesh increased to 77364.

It was not possible to reach appropriate results of A' and B' with any of the two turbulence models. In the case of $k-k_L-\omega$, it was only possible to reach good results for B', because there was a shift in phase of almost $90^o$ in the force curve in relation to the disk motion, resulting in A' near zero. A similar problem occurred for the $k-\omega-$ SST model. This time there was an increase in phase shift as KC increased, resulting in a decrease in A' for higher values of KC, which is the opposite behaviour in comparison with the experimental data. It is important to mention that the resulting force curve, for both models, may have similar maximum and minimum values in relation to the experimental data, but since there is a large shift phase in the forces, the dimensionless coefficients will not be similar.

The results of the laminar simulations of the dimensionless A' and B' are presented with the experimental data of (Tao and Dray, 2008) in Fig. 8. The black dashed line is the interpolation of the numerical data by a first order polynomial in A' and a second order in B'. From the figure, it is possible to see that the results are similar, but for A' the numerical

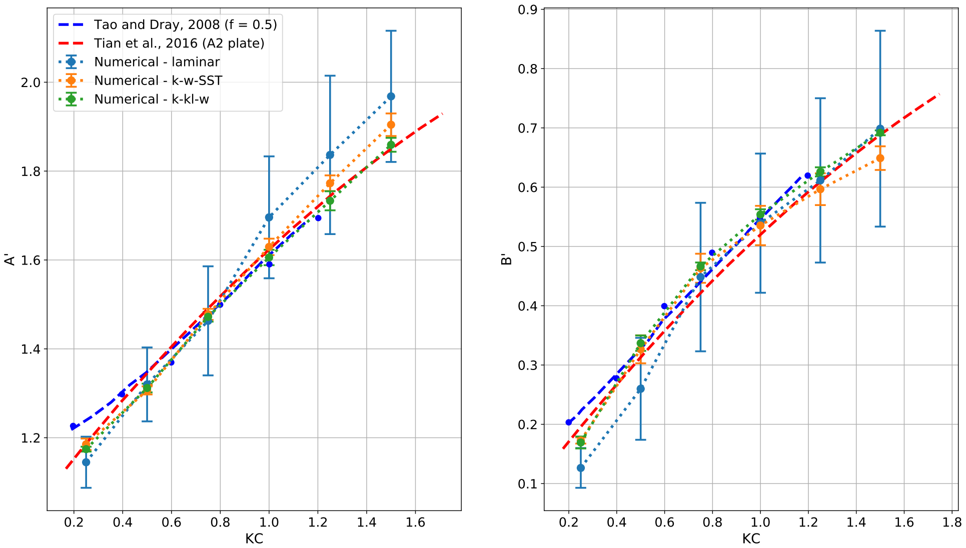

Figure 7. Result comparison for the simulations with solid plate using mesh M2

interpolation slope is different from the experimental.

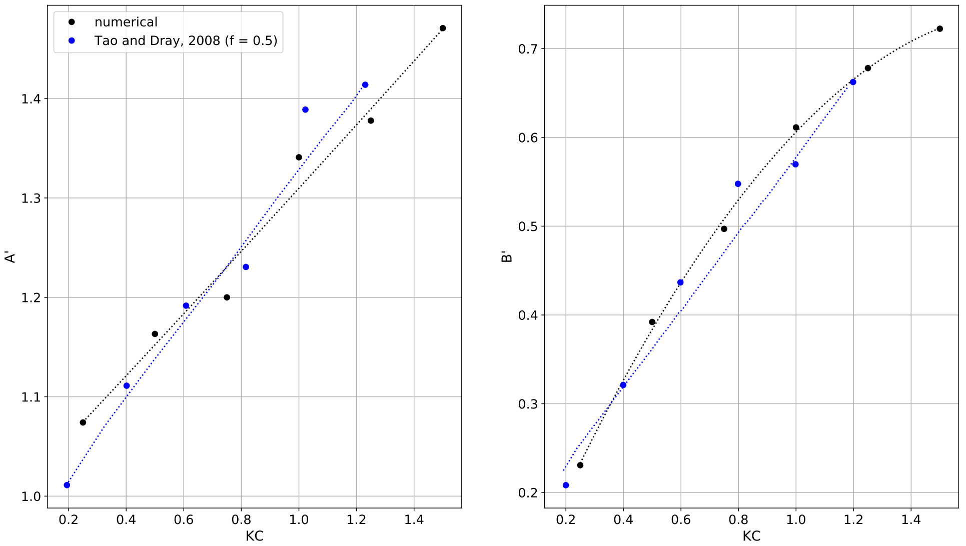

Figure 8. Result comparison for the simulations with 5% porosity and laminar viscous model

Figure 9 shows a comparison of the curl in the z direction, the velocity and the pressure field for the solid disk and the 5% porosity disk, with KC = 0.75, with laminar viscous model. In the figure the disk is on one extreme of its movement, with velocity equals to zero and maximum displacement, A. Comparing the curl results, it is possible to see that the top edge in the porous disk generates vortexes, likewise the solid one. However, there is no generation of curl inside or by the flow that pass through the porous zone. In the real scenario, there would be smaller vortexes being generate by the holes in the porous disk, thus, the adopted porous model used simplifies the flow field across the media. The pressure field comparison shows that the pressure is similar in both simulations. In the porous disk, pressure gradually decreases inside the region, due to Darcy's law, but there is no other major change comparing with the solid disk field. Comparing the velocity field of both simulations, velocities near the tip of the solid disk are higher than in the porous region tip. Also, the velocities are more evenly distributed near the porous disk simulation in relation to the solid disk, even though, there are no major changes in the velocity field inside the porous region.

## 7. CONCLUSION

The present paper showed a first analysis of CFD forced oscillation simulations using porous media in a disk geometry. In both proposed study cases there was good agreement with experimental results, but for the main objective of the paper there were some problems related to the models selected for the porous simulations.

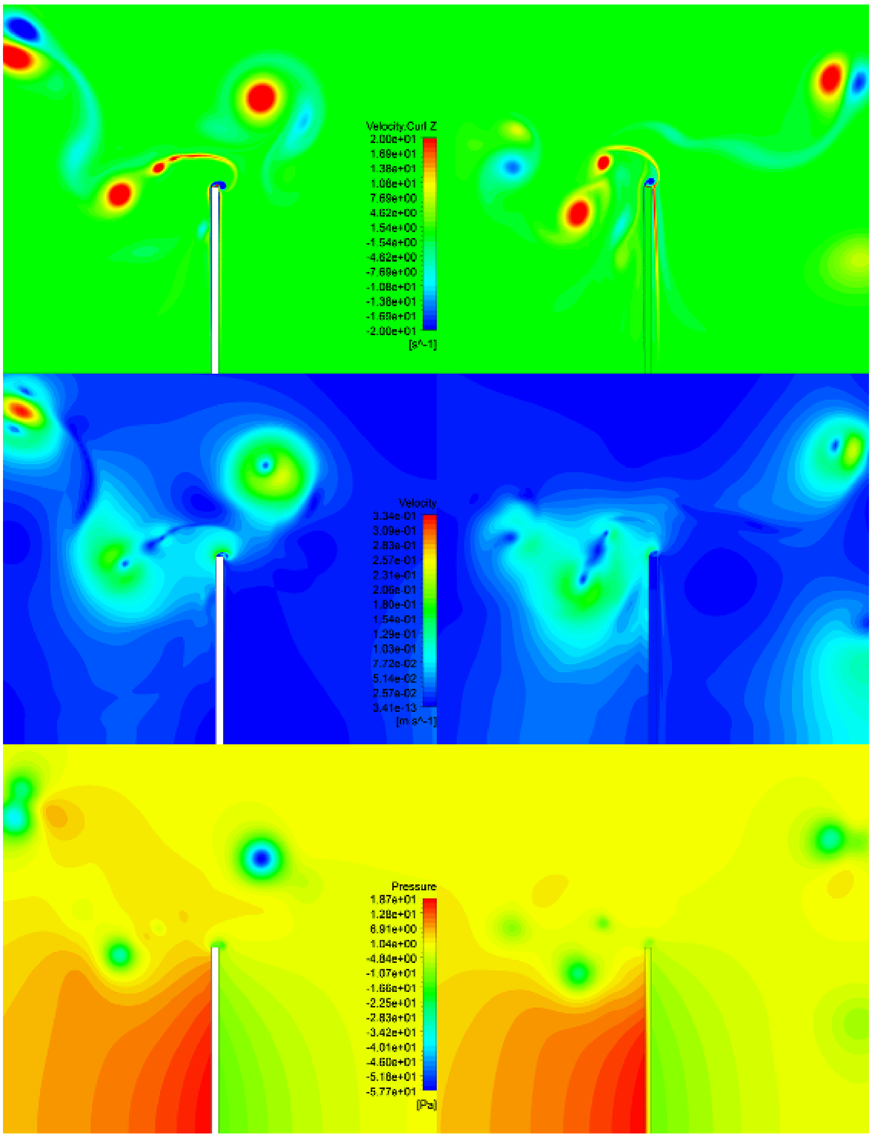

Figure 9. Z-Curl (top), velocity field (middle) and pressure field (bottom) comparison for the solid disk (left) and 5% porosity disk (right) [KC = 0.75]

The first problem encountered was related to the use of the physical velocity inside the porous media, which could give more realistic and accurate results inside the region. In this simple case scenario the superficial velocity was sufficient to solve the problem. The second problem occurred when the turbulence models were used in the porous media simulations. It was not possible to obtain meaningful hydrodynamic coefficients from them, due to the shift in the resulting force curve. For large subsea equipment, the Reynolds number in the flow will be much larger leading to turbulent flow, and so, these models will have to be used. There are two things to be tested in following works, one is to set the porous region as a laminar zone, when the porosity is small. By doing this, it is assumed that the Reynolds number in relation to the pores is bellow 1. The second option is to try to modify the turbulence models inside these regions, as done by Yan (2011).

Yet, from the results, it was possible to represent the flow through a more complex geometry using the porous media model, but with simplifications on the resulting flow.

On the next stages of this work, it will be also interesting to simulate more porosities, geometries, and the use of regions with different porosities and permeabilities; because the major objective of these works are to be able to simplify a subsea equipment with sets of regions with different geometries, porosities and permeabilities and achieve meaningful hydrodynamic coefficients for forced oscillation motion.

## 8. ACKNOWLEDGEMENTS

The authors would like to thank the Fundação de Apoio ao Instituto de Pesquisas Tecnológicas (FIPT).

## 9. REFERENCES

ANSYS, 2018. “Fluent 19.2 user′s guide”. ANSYS Web page. 28 Mar. 2019 <https://www.ansys.com>.

ASME, 2009. *Standard for Verification and Validation in Computational Fluid Dynamics and Heat Transfer*. American Society of Mechanical Engineer, New York.

Das, M.K., Mukherjee, P.P. and Muralidhar, K., 2018. *Modeling Transport Phenomena in Porous Media with Applications*. Springer International Publishing, Cham, Switzerland, 1st edition.

Dütsch, H., Durst, F., Becker, S. and Lienhart, H., 1998. “Low reynolds number flow around an oscillating circular cylinder at low keulegan carpenter numbers”. *Journal of Fluid Mechanics*, Vol. 360, pp. 249–271.

Eça, L., Hoekstra, M. and Vaz, G., 2015. “Verification of solutions in unsteady flows”. In *ASME Verification & Validation 2015 Symposium*. Las Vegas, USA.

Eça, L., Vaz, G. and Hoekstra, M., 2010. “Code verification, solution and validation in rans solvers”. In *Proceedings of the ASME 29th International Conference on Ocean, Offshore and Arctic Engineering - OMAE 2010*. Shanghai, China.

Ghozlani, B., Hafsia, Z. and Maalel, K., 2012. “Numerical study of flow around an oscillating diamond prism and circular cylinder at low keulegan-carpenter number”. *Journal of Hydrodynamics*, Vol. 24, No. 5, pp. 767–775.

Keulegan, G.H. and Carpenter, L.H., 1958. “Forces on cylinders and plates in an oscillating fluid”. *Journal of Research of the National Bureau of Standards*, Vol. 60, No. 5, pp. 423–440.

Kjemperud, S., 2011. *Hydrodynamic coefficients for wellhead structures*. Ph.D. thesis, Norwegian University of Science and Technology, Trondheim, Norway.

Meeker, W.Q., Hahn, G.J. and Escobar, L.A., 2017. *Statistical intervals : a guide for practitioners and researchers*. John Wiley & Sons, Inc., New Jersey, USA, 2nd edition.

Menter, F.R., 1994. “Two-equation eddy-viscosity turbulence models for engineering applications”. *AIAA Journal*, Vol. 32, No. 8, pp. 1598–1605.

Menter, F.R., Langtry, R.B., Likki, S.R., Suzen, Y.B., Huang, P.G. and Völker, S., 2006. “A correlation-based transition model using local variables-part i: Model formulation”. *Journal of Turbomachinery*, Vol. 128, pp. 413–422.

Minguez, M., Aljarah, R., Malassagne, A., Jebali, A. and Luppi, A., 2015. “Cfd & basin test benchmarks for subsea lift analaysis”. In *Offshore Technology Conference - OTC 2015*. Houston, USA.

Sarpkaya, T. and Isaacson, T., 1981. *Mechanics of Wave Forces on Offshore Structures*. Van Nostrand Reinhold Co., New York, 1st edition.

Tao, L. and Dray, D., 2008. “Hydrodynamic performance of solid and porous heave plates”. *Ocean Engineering*, Vol. 35, pp. 1006–1014.

Tao, L. and Thiagarajan, K., 2003. “Low kc flow regimes of oscillating sharp edges i. vortex shedding observation”. *Applied Ocean Research*, Vol. 25, No. 1, pp. 21 – 35.

Tatsuno, M. and Bearman, P.W., 1990. “A visual study of the flow around an oscillating circular cylinder at low keulegan-carpenter numbers and low stokes numbers”. *Journal of Fluid Mechanics*, Vol. 211, pp. 157–182.

Tian, X., Tao, L., Li, X. and Yang, J., 2017. “Hydrodynamic coefficients of oscillating flat plates at $0.15 \leq kc \leq 3.15$”. *Journal of Marine Science and Technology*, Vol. 22, No. 1, pp. 101–113.

Wadhwa, H. and Thiagarajan, K.P., 2009. “Experimental assesment of hydrodynamic coefficients of disks oscillating near a free surface”. In *Proceedings of the ASME 2009 28th International Conference on Ocean, Offshore and Arctic Engineering - OMAE 2009*. Honolulu, USA.

Walters, D.K. and Cokljat, D., 2008. “A three-equation eddy-viscosity model for reynolds-averaged navierâĂŞstokes simulations of transitional flow”. *Journal of Fluids Engineering*, Vol. 130, No. 12, pp. 121401–14.

Yan, Y., 2011. *Development of a coupled CFD-System-code capability (with a modified porous media model) and its applications to simulate current and next generation reactors*. Ph.D. thesis, University of Illinois, Urbana-Champaign, USA.

## 10. RESPONSIBILITY NOTICE

The authors are the only responsible for the printed material included in this paper.